

Toward the working mechanisms of tin oxide as buffer layer in perovskite/silicon tandem solar cells

Cite as: Appl. Phys. Rev. **12**, 021403 (2025); doi: [10.1063/5.0255418](https://doi.org/10.1063/5.0255418)

Submitted: 29 December 2024 · Accepted: 21 March 2025 ·

Published Online: 4 April 2025




View Online



Export Citation



CrossMark

Qing Yang,^{1,2}  Karsten Bittkau,¹  Benjamin Klingebiel,¹  Thomas Kirchartz,^{1,3}  Uwe Rau,^{1,2,a)}  and Kaining Ding^{1,2,a)} 

AFFILIATIONS

¹IMD-3 Photovoltaics, Forschungszentrum Jülich GmbH, Wilhelm-Johnen Straße, 52425 Jülich, Germany

²Jülich Aachen Research Alliance (JARA-Energy) and Faculty of Electrical Engineering and Information Technology, RWTH Aachen University, Schinkelstr. 2, 52062 Aachen, Germany

³Faculty of Engineering and CENIDE, University of Duisburg-Essen, Carl-Benz-Str. 199, 47057 Duisburg, Germany

^{a)}Authors to whom correspondence should be addressed: u.rau@fz-juelich.de and k.ding@fz-juelich.de

ABSTRACT

Tin oxide (SnO_x), a buffer layer commonly used to protect both the electron transport layer and the perovskite layer from sputtering-induced damage during the deposition of transparent conductive oxide in the top cell of perovskite-related tandem solar cells, is considered essential for achieving high efficiencies. Here, we systematically investigate the impact of SnO_x on single-junction perovskite solar cells to understand the working mechanism of SnO_x in the perovskite top cells. We discuss the correlation between the SnO_x process and the photovoltaic parameters using steady-state photoluminescence, external quantum efficiency, space-charge-limited current measurements, and numerical simulations. We observe that the efficiency increased with thicker SnO_x and the results suggest that thicker SnO_x not only decreases the series resistance of perovskite solar cells but also has the potential to suppress nonradiative recombination. The improved buffer layer is finally used to produce a perovskite/silicon tandem solar cell with an efficiency of 32.84% (with a corresponding efficiency of 31.81% calculated using the short-circuit current density from the external quantum efficiency measurements).

© 2025 Author(s). All article content, except where otherwise noted, is licensed under a Creative Commons Attribution (CC BY) license (<https://creativecommons.org/licenses/by/4.0/>). <https://doi.org/10.1063/5.0255418>

I. INTRODUCTION

Over the last year, perovskite/silicon tandem solar cells have made significant progress in terms of efficiency.^{1,2} The latest champion efficiency certified by the European Solar Test Installation (ESTI) is 34.6%,³ with an active area of 1 cm^2 , which was achieved by LONGI. To obtain high efficiency, a robust buffer layer is essential to protect the underlying stacks from sputter damage due to transparent electrode deposition⁴ during perovskite/silicon tandem solar cell manufacturing. The mechanisms of sputter damage and effective methods for mitigating the damage have been thoroughly studied.^{4,5} In general, either lowering the sputtering power⁶ during the sputtering process or inserting a buffer layer⁷ before the start of the sputtering process can effectively remove sputter-induced damage and prevent the formation of S-shaped current density vs voltage (JV) curves. Transparent conductive oxides (TCOs) are widely used as transparent electrodes because of their high optical transparency and excellent

electrical conductivity.⁸ However, because the balance between the optical and electrical properties of TCOs might be disrupted by lowering the sputtering power, resulting in additional parasitic optical absorption losses, in most cases, a buffer layer is used to mitigate sputter damage. Another unavoidable issue accompanying sputtering power reduction is the dramatic increase in the sheet resistance of TCOs such as indium tin oxide (ITO),⁷ which is among the preferred choices for transparent electrodes in perovskite-related tandem solar cells. This increase in sheet resistance resulted in an increase in the series resistance of the solar cell. In our specific scenario, the decrease in the sputtering power from 50 to 30 W resulted in a dramatic increase in the sheet resistance of the 110-nm-thick ITO film, increasing it from 150 to 3000 Ω/sq . Despite the effective reduction in sputter damage, ITO films exhibiting such high sheet resistance are no longer suitable for application as transparent electrodes in perovskite-related tandem solar cells. Therefore, nearly all perovskite/silicon tandem solar

cells, whose efficiency is documented in the NREL chart of best research-cell efficiencies, incorporate a buffer layer prior to the deposition of TCOs.^{2,9}

In perovskite/silicon tandem solar cells with an inverted structure (pin), the commonly used buffer layer is tin oxide (SnO_x), which is often deposited by atomic layer deposition (ALD) onto the electron transport layer (ETL) C_{60} . Tandem solar cells with inverted (pin) perovskite top cells have been proven to show much higher efficiencies than those with regular (nip) layer stacks;⁷ the structures of single-junction perovskite solar cells (PSCs) and perovskite-related tandem solar cells discussed in this work are only inverted structures (pin). In 2017, Bush *et al.*⁷ first employed SnO_x as a buffer layer before ITO sputtering in rear-side-textured perovskite/SHJ solar cells. In the following year, Ballif *et al.* employed SnO_x as a buffer layer in both front-side textured perovskite/TOPCon tandem solar cells¹⁰ and double-side textured perovskite/SHJ solar cells.¹¹ Since then, SnO_x has become a commonly used buffer layer in perovskite/silicon tandem solar cells to protect the underlying organic stack from sputter damage, although the choice of transparent electrodes varies from ITO to IZO.^{12,13}

Although SnO_x has been widely used as a sputter buffer layer in perovskite/silicon tandem solar cells, independent research has rarely been conducted on its working mechanisms, either for applications in tandem solar cells or single-junction devices, including opaque PSCs and semi-transparent PSCs. In 2018, Bent *et al.*¹⁴ reported detailed research on the ALD precursor-perovskite interactions of the ALD- SnO_x system, which highlighted the role of organic fullerenes at the perovskite/ SnO_x interface in semi-transparent PSCs but did not mention the role of the buffer layer. Two years later, Huang *et al.*¹⁵ reported the ambipolar carrier transport property of SnO_x enabled by the incomplete oxidation of tin ($x = 1.76$); however, it acted as an interconnection layer for all-perovskite tandem solar cells instead of a buffer layer for the subcells. Generally, when SnO_x is used as a buffer layer in perovskite/silicon tandem solar cells, there is a lack of knowledge whether it purely provides physical protection to the underlying stacks against sputter damage. Furthermore, it is unclear whether the $\text{C}_{60}/\text{SnO}_x$ interface affects carrier extraction, or whether the insertion of SnO_x alters the electrical properties or passivation quality of the tandem device.

In perovskite/silicon tandem solar cells, the SnO_x buffer layer belongs to the perovskite top cell. Thus, in this work, we systematically investigated the impact of SnO_x on single-junction PSCs as a reference to understand the working mechanism of SnO_x in perovskite top cells, which is not only simpler and more intuitive than a direct investigation in tandem devices because of its complicated layer stack but also guides us in optimizing the performance of tandem solar cells. Changes in the photovoltaic parameters were analyzed individually to gain insight into the performance improvement as a function of the SnO_x thickness for single-junction devices. In addition, the steady-state photoluminescence (ssPL) spectra and photoluminescence quantum efficiencies $Q_{\text{e,lum}}$ of the PSCs were studied. The aim was to understand the impact of SnO_x on nonradiative recombination when the film thickness varies. Ultraviolet photoelectron spectroscopy (UPS) measurements were performed to monitor the energy levels of all the materials, and numerical simulations were performed using drift-diffusion simulation software (SCAPS)¹⁶ to analyze whether the thickness of SnO_x affects the band alignment in PSCs. Moreover, we applied a recently developed method¹⁷ of using space-charge-limited

current (SCLC) measurements to our perovskite solar cells to study the relative shift of the work function of SnO_x , which consequently affects the charge carrier extraction at the ETL side. Our study aims to understand the working mechanisms of SnO_x as a buffer layer in perovskite top cells.

This paper is structured as follows. A review of the existing literature relevant to SnO_x buffer layer lays the foundation for this study (Sec. I). We present the solar cell performance as a function of the SnO_x film thickness (Sec. II). The dependence of V_{OC} and J_{SC} on buffer layer thickness is discussed using the corresponding ssPL results (Sec. III) and external quantum efficiency upon dual illumination (Sec. IV), respectively. The dependence of FF on buffer layer thickness is the most complex and difficult chapter to analyze (Sec. V); thus, it has been divided into four sub-chapters for providing a comprehensive understanding. The ideality factor and comparison between various FF s offer insights into the FF losses (Sec. V A). We construct the band diagram for cells using the UPS results and preliminary drift-diffusion simulation to try to understand the mechanisms of SnO_x as buffer layer (Sec. V B). SCLC allows us to quantitatively evaluate the differences between the work function of SnO_x without taking into account the absolute errors embedded in the UPS measurements, which improves the definition for simulations (Sec. V C). The comparison of the measured FF s to the results of the improved device simulations shows a good match, suggesting that the information in the band diagram is reliable and can be used to explain the working mechanisms (Sec. V D). The output performance of a tandem solar cell employing a SnO_x buffer layer is presented (Sec. VI). Finally, the key findings and their contributions are summarized (Sec. VII).

II. SOLAR CELL PERFORMANCE

In this work, we fabricated semi-transparent PSCs with an inverted structure (pin) as a function of the thickness of SnO_x buffer layer, wherein the thickness increased from 5 to 25 nm in increments of 5 nm. Figure 1 presents the solar cell parameters, that is, the efficiency (η), short-circuit current density (J_{SC}), fill factor (FF), and open-circuit voltage (V_{OC}), as functions of SnO_x film thickness. We observe that the average η increased from 12.1% at 5 nm to a maximum value of 17.5% at 15 nm. A further increase in SnO_x thickness led to a negligible influence on solar cell performance. As the SnO_x film thickness increased from 5 to 25 nm, the trend of the J_{SC} and FF aligned with that of η , while the average V_{OC} exhibited a slight enhancement. Our previous findings⁵ revealed that the implementation of an SnO_x buffer layer with a critical thickness of 15 nm effectively mitigated sputter damage during ITO deposition, as it guarantees the presence of adequate phonon scattering events within the SnO_x layer. Consequently, the energy carried by phonons that ultimately reach the perovskite surface is too low to initiate chemical bond dissociation. However, we observe a pronounced S-shape in the JV curves of semi-transparent PSCs employing a 5-nm-thick SnO_x buffer layer. The S-shape likely originates from sputter damage to the underlying perovskite/ C_{60} stack. These results indicate that the performance of semi-transparent PSCs employing a 20-nm or 25-nm-thick SnO_x buffer layer is no longer compromised by sputter damage but is exclusively affected by the SnO_x film thickness, as shown in Fig. 1(a). Conversely, the increase in η as the thickness of SnO_x increases from 5 to 15 nm should be affected by both the variation in buffer layer thickness and the mitigation of the sputter damage.

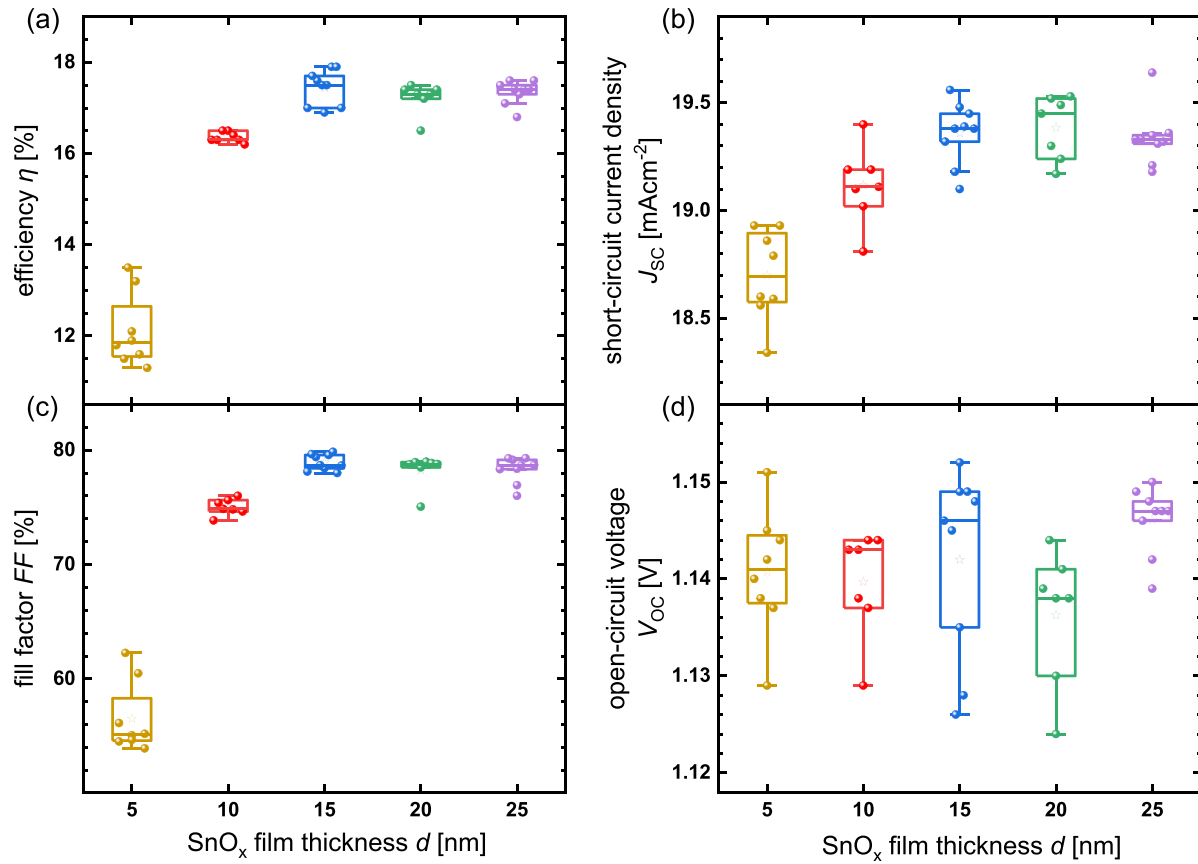


FIG. 1. Statistics of (a) η , (b) J_{SC} , (c) FF , and (d) V_{OC} of semi-transparent perovskite solar cells as a function of SnO_x film thickness. The device configuration is glass/ITO/MeO-2PACz/perovskite/PEAI/ C_{60} / SnO_x /ITO/Ag. Statistical data were obtained from current-voltage measurements, which allows for evaluating the evolution of semi-transparent solar cell parameters as the SnO_x thickness increases from 5 to 25 nm and the ITO-induced sputter damage was mitigated accordingly. The solar cell performance reached saturation at 15 nm.

To independently examine the influence of SnO_x film thickness on solar cell performance, we fabricated opaque PSCs with an inverted structure (pin), wherein a SnO_x buffer layer was incorporated and positioned between the ETL, C_{60} , and Ag electrode. This configuration enables the elimination of the considerable detrimental effects of the sputter damage associated with ITO deposition. The thickness of SnO_x was incrementally increased from an initial 5 nm to a critical value of 15 nm in steps of 5 nm, as further increase in thickness to 20 or 25 nm resulted in negligible degradation or enhancement in solar cell performance. In contrast to the thermally evaporated BCP buffer layer, the SnO_x layer was deposited using ALD, featuring a stable deposition rate of 1.5 Å/cycle. Thus, the film thickness was precisely controlled by the number of deposition cycles. In Fig. 2, the results illustrate that the average η of opaque PSCs increased from 17.4% at 5 nm to a maximum value of 18.8% at 15 nm. To understand the working mechanism of SnO_x at the interface of C_{60} /Ag in inverted PSCs, the changes in the photovoltaic parameters with SnO_x film thickness were analyzed individually using various characterization methods. It is the aim of our study to understand the dependency of each solar cell parameter on the buffer layer thickness, starting with V_{OC} .

III. DEPENDENCE OF V_{OC} ON BUFFER LAYER THICKNESS—REDUCTION OF NONRADIATIVE RECOMBINATION

Photoluminescence (PL) spectroscopy is a suitable tool for quantitatively evaluating changes in radiative and unwanted nonradiative recombination by measuring the emission of photons from a semiconductor that have been created by radiative recombination and comparing absolute or relative PL intensities as a function of sample geometry or processing without requiring electrical contacts.¹⁸ Thus, we studied the absolute PL spectra and quantum yields of the devices as a function of SnO_x film thickness. From the absolute PL intensities, we determine the average quasi-Fermi level splitting^{18–20} ΔE_F by using

$$\Delta E_F = \Delta E_{F,\text{rad}} + kT \ln\{Q_{e,\text{lum}}\} \quad (1)$$

assuming a flat quasi-Fermi level where the radiatively limited $\Delta E_{F,\text{rad}}$ refers to the maximum achievable Fermi level splitting in the absence of nonradiative (defect) recombination that can be determined using detailed balance arguments akin to those used for the Shockley–Queisser model.²¹ The external quantum efficiency of the PL emission $Q_{e,\text{lum}} = \frac{Y_{\text{em}}}{Y_{\text{rec}}}$, defined as the ratio of the emitted photon flux (Y_{em}) to

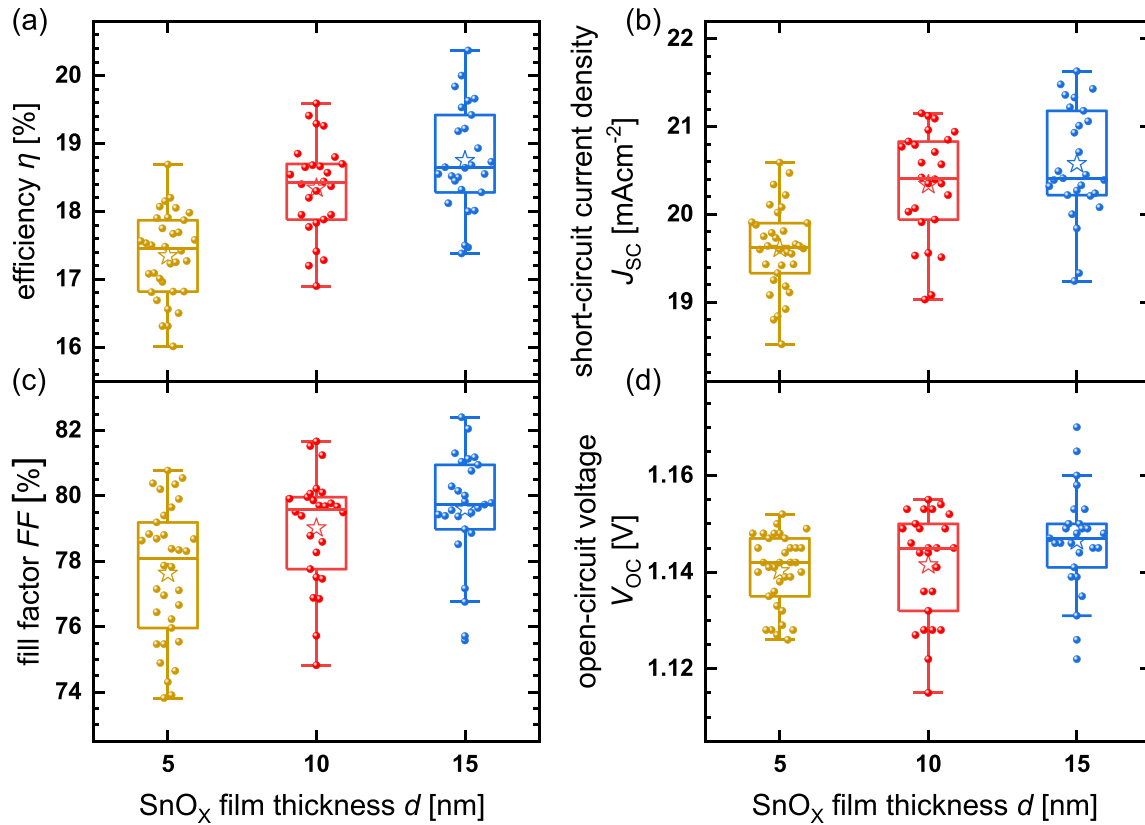


FIG. 2. Statistics of (a) η , (b) J_{SC} , (c) FF , and (d) V_{OC} of opaque perovskite solar cells as a function of SnO_x film thickness. The device configuration is glass/ITO/MeO-2PACz/perovskite/PEAI/ C_{60} / SnO_x /Ag. Statistical data allows for evaluating the evolution of opaque solar cell parameters purely as the SnO_x thickness increases from 5 nm to the saturated value of 15 nm. Further increments in thickness did not enhance device performance in the absence of ITO-induced sputter damage, as demonstrated in Fig. 1.

the recombination flux (Y_{rec}), can be directly obtained through experiments. k and T are the Boltzmann constant and the temperature, respectively. Figures 3(a)–3(c) show the PL spectra of the representative devices at open-circuit, the ΔE_F and the corresponding $Q_{e,\text{lum}}$ values of the PSCs as functions of SnO_x film thickness. As the SnO_x thickness increases from 5 to 15 nm, the PL intensity, ΔE_F , and $Q_{e,\text{lum}}$ increase, suggesting a higher fraction of radiative recombination and a lower fraction of nonradiative recombination. The results demonstrate that thick SnO_x films reduce nonradiative recombination in PSCs, which explains the trend of slightly higher V_{OC} for thicker SnO_x films, as shown in Fig. 2(d).

According to our previous work,⁵ SnO_x is likely to exhibit a significantly lower work function than bare C_{60} , which will result in an upward shift of the Fermi level at the perovskite/ C_{60} interface toward the conduction band of C_{60} . In the present study, the increase in SnO_x film thickness is likely to reduce the work function of bare SnO_x , suggesting that the Fermi level at the perovskite/ C_{60} interface will be closer to the conduction band of C_{60} in the perovskite solar cells employing a thicker SnO_x buffer layer compared to the 5 nm counterpart, ultimately enabling the presence of a larger quasi-Fermi level splitting, as shown in Fig. 3(b). As the SnO_x film thickness increases, the upward shift of the Fermi level at the perovskite/ C_{60} interface reduced the hole concentration in the perovskite at the interface, thereby reducing the

nonradiative recombination rate at the perovskite/ C_{60} interface. Consequently, the PL intensity was enhanced as the SnO_x film thickness increased. The characterization of energy levels and the device simulations presented in Sec. V will substantiate this speculation.

IV. DEPENDENCE OF J_{SC} ON BUFFER LAYER THICKNESS—IMPROVEMENT OF INTERFACE PASSIVATION

Figure 2(b) shows an increase in J_{SC} with increasing SnO_x thickness. To obtain a better insight into the optical enhancement, external quantum efficiency ($Q_{e,\text{PV}}$) measurements were performed on representative devices with different SnO_x film thicknesses. Representative $Q_{e,\text{PV}}$ and 1-reflectance (1-R) are shown in Fig. 4. We observed that thicker SnO_x exhibited an enhanced optical response at wavelengths between 490 and 730 nm, but the corresponding 1-R of each representative device did not show a significant difference over the wavelength range. This demonstrates that the reflectance was not the dominant reason for the $Q_{e,\text{PV}}$ enhancement with thicker SnO_x .

For any wavelength, there is more absorption on the incident side than on the opposite side, which roughly follows the Lambert–Beer law.²² Based on our previous work,²³ there was a much higher fraction of generation for long wavelengths at the rear side than at short wavelengths. Therefore, the specific $Q_{e,\text{PV}}$ response in the long-wavelength

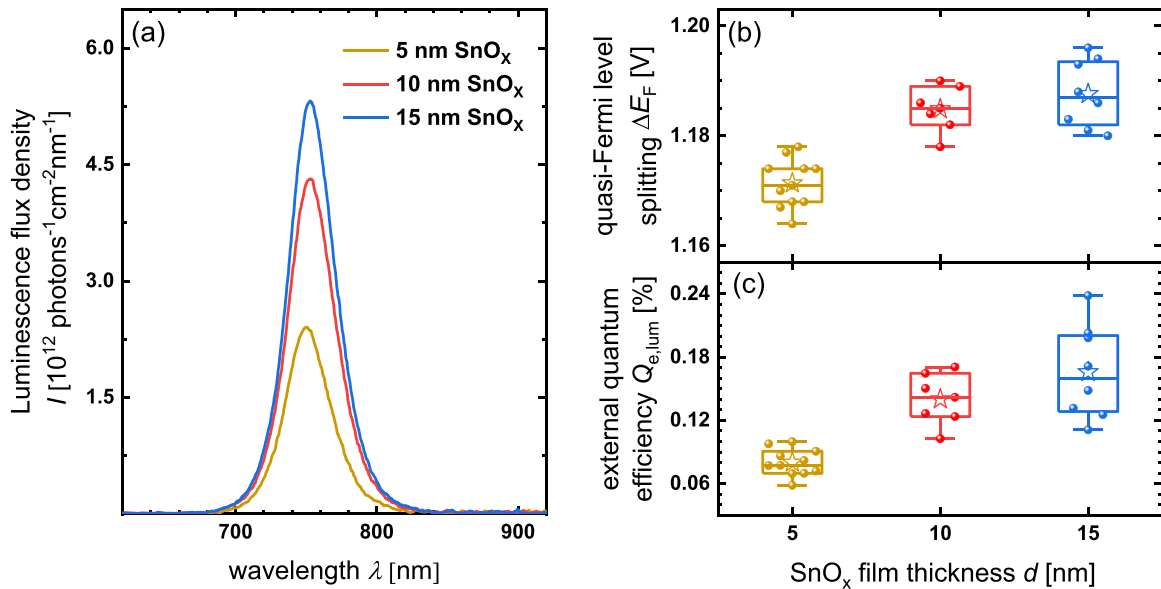


FIG. 3. (a) PL spectra of the representative opaque perovskite solar cells incorporating 5, 10, and 15 nm SnO_x at open circuit. Statistics of (b) ΔE_F and (c) $Q_{e,\text{lum}}$ for opaque perovskite solar cells as a function of SnO_x film thickness. PL intensity, average quasi-Fermi level splitting, and external quantum efficiency of the PL emission derived from the contactless PL measurement enable the comparison of the strength of radiative and nonradiative recombination in completed devices incorporating a SnO_x buffer layer with increasing thickness. Thick SnO_x films reduce nonradiative recombination in opaque perovskite solar cells.

range depends on the illumination direction and susceptibility to the surface recombination velocity in the presence of slow carrier separation.²³ In the case of issues with the interface passivation quality on one side, the separation of electron-hole pairs on this side suffers.

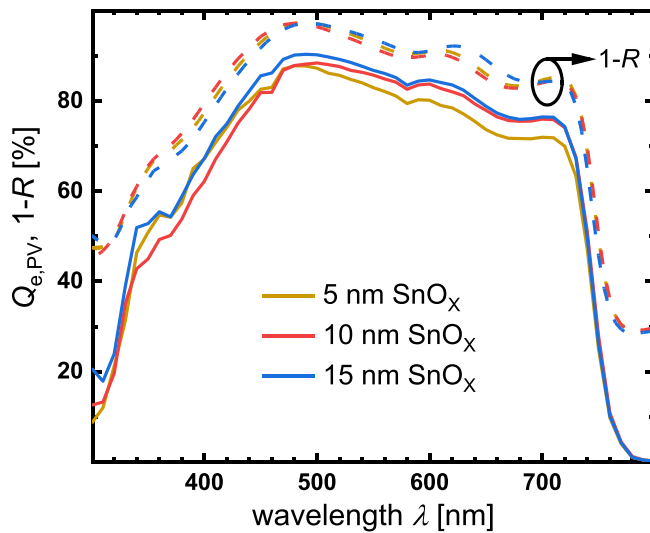


FIG. 4. $Q_{e,\text{PV}}$ and $1-R$ of the representative opaque perovskite solar cells incorporating 5, 10, and 15 nm SnO_x measured from the HTL side, which are obtained from the quantum efficiency and reflectance measurements, respectively. The spectra allows to compare the optical response over the entire wavelength range. Thick SnO_x films enhance the $Q_{e,\text{PV}}$ response of opaque devices at long wavelengths between 490 and 730 nm without affecting the reflectance.

Consequently, recombination occurs, resulting in a reduction in the effective collection and a failure in current generation. This deficiency ultimately affects the quantum efficiency of long-wavelength light.²³ If light enters the solar cell on the poorly passivated side, the quantum efficiency across the entire wavelength range will suffer from its negative impact.

In the case of opaque PSCs, $Q_{e,\text{PV}}$ were measured purely from the HTL side of the representative devices. As a result, the optical response at long wavelengths was enhanced for thicker SnO_x , suggesting that the collection of electrons became more efficient compared to their thin counterparts. The absence of differences at short wavelengths illustrates that hole collection was almost unaffected. Therefore, we speculate that the reason for the enhanced optical response is perhaps that the interface passivation quality close to the ETL side was improved by thicker SnO_x . To substantiate this speculation, it is necessary to measure $Q_{e,\text{PV}}$ from both sides of the device, which will help to determine whether the wavelength region of optical response enhancement undergoes any changes when the direction of illumination is altered. Considering that the ETL side of the PSCs was fully covered by the Ag electrode, JV and $Q_{e,\text{PV}}$ measurements can only be performed from the HTL side. To conduct double-sided measurements, the opaque electrode was replaced with TCOs, and indium zinc oxide (IZO) was used to fabricate semi-transparent perovskite solar cells. Therefore, it became feasible to illuminate both the ETL and HTL sides, and the thickness of SnO_x remained the sole variable in the preparation of the semi-transparent devices (see [supplementary material](#) for more details).

$Q_{e,\text{PV}}$ measurements of representative semi-transparent perovskite solar cells were performed from both the HTL and ETL sides, and the results are shown in [Figs. 5\(a\) and 5\(b\)](#) with the $1-R$ plotted together. Regardless of the illuminated side, the $Q_{e,\text{PV}}$ response

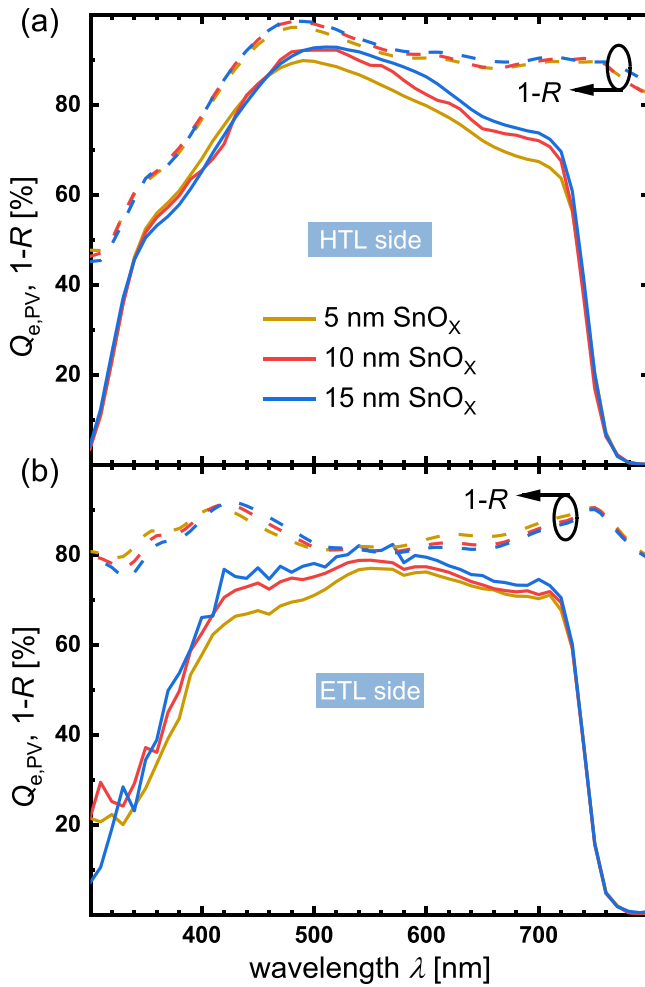


FIG. 5. $Q_{e,PV}$ and $1-R$ of the representative semi-transparent perovskite solar cells incorporating 5, 10, and 15 nm SnO_x measured from the (a) HTL and (b) ETL sides. Upon HTL-side measurement, the thick SnO_x films enhance the $Q_{e,PV}$ response of semi-transparent devices at long wavelengths between 490 and 720 nm, which is consistent with that of the opaque devices; whereas the optical enhancement was observed over the entire wavelength range of 300–800 nm upon ETL-side measurement. In both cases, the reflectance did not exhibit a significant difference as a function of the SnO_x film thickness. Based on our previous work,²³ this phenomenon is most likely attributed to the improvements in interface passivation quality near the ETL side as SnO_x thickness increases.

exhibited an enhancement as the thickness of SnO_x increased. When $Q_{e,PV}$ was measured from the HTL side, the optical response enhancement only occurred at relatively long wavelengths between 490 and 720 nm, and no notable difference was observed at short wavelengths below 490 nm, as shown in Fig. 5(a). The wavelength range of the optical response enhancement matches well with that of opaque PSCs, as depicted in Fig. 3. However, when $Q_{e,PV}$ was measured from the ETL side, the optical response was enhanced over the entire wavelength range of 300–800 nm, as shown in Fig. 5(b). These results illustrate that the wavelength range of optical response enhancement changes significantly after the incident light surface is switched from the HTL

side to the ETL side.²³ To investigate whether the changes were affected by the variations in the intrinsic optical properties of the semi-transparent devices, reflectance measurements were subsequently conducted. The reflectance of the finished devices at short wavelengths upon HTL-side measurement did not show a significant difference over the wavelength range as the SnO_x film thickness increased. When the reflectance was measured from the ETL side, the curves were slightly red-shifted as the thickness of SnO_x increased, but did not exhibit a significant difference over the wavelength range of 300–800 nm. These results indicate that the changes in the optical response enhancement were not primarily due to reflectance when the illumination direction was altered. Combined with the results of our previous analysis, these changes are most likely attributed to the improvements in the interface passivation quality near the ETL side. This is because of the reduction in nonradiative recombination as the SnO_x film thickness increased. For illumination from the HTL side, the visible light generates electron–hole pairs close to the HTL/perovskite interface. In contrast, only the infrared radiation leads to the generation of charge carriers close to the ETL/perovskite interface. Because a thicker SnO_x suppressed nonradiative recombination at the ETL side, $Q_{e,PV}$ enhancement primarily occurred at long wavelengths. In contrast, when the incident light surface was on the ETL side, light over the entire wavelength range generated carriers near the SnO_x layer. Thus, owing to the inhibitory effect of the thicker SnO_x film on nonradiative recombination, the optical response across the wavelength range of 300–800 nm was improved.

The above analysis of V_{OC} and J_{SC} indicates that a thick SnO_x film might improve the interface passivation quality by reducing non-radiative recombination. The following study on thickness-dependent FF might help us to determine the location of recombination more precisely.

V. DEPENDENCE OF FF ON BUFFER LAYER THICKNESS—REDUCTION OF TRANSPORT LOSSES

A. Fill factor and ideality factor

In PSCs with an inverted structure of glass/ITO/HTL/perovskite/ C_{60} /BCP/Ag, FF decreased as the thickness of BCP increased, which was generally attributed to charge accumulation²⁴ and poor electrical contact.²⁵ However, when the BCP was replaced by a SnO_x film, the trend was completely reversed, where FF increased as the SnO_x film thickness increased from 5 to 15 nm, as shown in Fig. 2(c). Because the sheet resistance (R_{SH}) of both BCP and SnO_x thin films exceeds the measurement range (10 m Ω /sq–10⁴ Ω /sq) of the four-probe method²⁶ (MR-1 produced by Schuetz Messtechnik GMBH), both are poor conductors with poor conductivity. Theoretically, the thicker the insulating film, the higher the risk of a low FF . In the following, we discuss possible reasons for the reversed trend in FF with buffer layer thickness in the case of SnO_x . This will help understand the possible sources of FF losses in PSCs.

In the absence of resistive losses, the upper limit on the FF is approximately given by²⁷

$$FF = \frac{v_{OC} - \ln(v_{OC} + 0.72)}{v_{OC} + 1}, \quad (2)$$

where the normalized open-circuit voltage $v_{OC} = (qV_{OC})/(n_{id}kT)$, with q being the elementary charge and n_{id} being the diode ideality factor. The value of FF given by this equation depends only on n_{id} , V_{OC} ,

and T . Other factors, such as the series and parallel resistances, were not considered in Eq. (2). The ideal FF (FF_{id}) is reached when n_{id} equals 1, which is limited only by radiative recombination and does not consider resistive losses. The impact of n_{id} on FF can also be estimated by varying its values in Eq. (2).

The ideality factor n_{id} , following from

$$n_{id} = \frac{q}{kT} J_{SC} \frac{dV_{OC}}{dJ_{SC}} \quad (3)$$

was determined by the measurement of the V_{OC} as a function of the light intensity.^{28,29} In PSCs, n_{id} varies between 1 and 2,^{30,31} and the value provides some information on the recombination mechanism. Ideality factors of one or close to one may originate from radiative band-to-band recombination of free charges, recombination via sufficiently shallow traps, and any recombination mechanism in a sufficiently doped semiconductor.³² In most lead-based perovskites doping densities are low,³³ luminescence quantum efficiencies are significantly below unity, and hence, ideality factors between 1 and 1.5 are most consistent with Shockley–Read–Hall (SRH) recombination via states that are more or less shallow. Ideality factors close to 2, in contrast, originate from trap-assisted recombination through mid-gap impurities in an intrinsic semiconductor.³² These states do not have to be in the bulk of the perovskite but can also be at the interfaces to electron and hole transport layers. The nonradiative recombination losses with $n_{id} > 1$ limit not only the V_{OC} of the devices but also the FF .

Parallel resistance can also result in FF losses because solar cells often exhibit shunt-like behavior under illumination, which is called photoshunting,³⁴ and is attributed to recombination currents that appear Ohmic, i.e., have an approximately linear J - V relation for a range of voltages. To quantify the FF losses due to a photoshunting, the JV curves of representative devices for different SnO_x thicknesses were shifted to the first quadrant by adding the respective J_{SC} , and are depicted together with the dark JV (JV_{dark}) curves using a logarithmic current axis, as shown in Fig. 6(b). The illuminated JV curves show a feature that resembles the effect of a low shunt resistance but is not visible in the JV_{dark} curves. The moderate slope in the lower voltage region is referred to as photoshunting, which results from slow carrier extraction at short circuits and low forward voltages,³⁴ resulting in a recombination current that acts as a shunt. The results demonstrate a significant decrease in the photoshunting as the thickness of SnO_x increases from 5 to 10 nm. A slight additional decrease was observed from 10 to 15 nm, suggesting that the PSCs employing 15 nm SnO_x might have the lowest recombination current. The results of drift-diffusion simulations revealed that the photoshunting is strongly dependent on the recombination velocity (S) at the perovskite/transporting layer interface in PSCs (Fig. S1). Based on the observations of the photoshunting, it was demonstrated once again that a thicker SnO_x film can effectively suppress carrier recombination at the ETL side, assuming that the S value at the HTL side is constant. These results match well with previous PL and $Q_{e,pv}$ results.

The transport losses of the charge carriers cause series resistance losses, which consist of bulk, contact, and lateral resistance losses. Pseudo- JV (pJV) curves are determined by the V_{OC} of the device at different illumination intensity and J_{SC} , which only reflects generation and recombination processes without the effect of the series resistances, because the net current is zero at open circuit. Therefore, the impact of the overall series resistance (R_s) on FF losses can be

accurately evaluated by calculating the pseudo- FF (pFF) of a complete device through intensity-dependent J_{SC}/V_{OC} measurements. The difference between pFF and FF represents the FF loss caused by R_s , which can be identified by ΔFF_{R_s} . In addition, the FF losses caused by $n_{id} > 1$ can be identified by ΔFF_{mid} , the difference between the pFF and FF_{id} extracted from the ideal JV curve (JV_{id}), where $n_{id} = 1$ and $R_s = 0$. ΔFF_{R_s} and ΔFF_{mid} were expressed by the following equations:

$$\Delta FF_{R_s} = pFF - FF, \quad (4)$$

and

$$\Delta FF_{mid} = FF_{id} - pFF. \quad (5)$$

To intuitively compare the FF losses due to the nonideal n_{id} and R_s , the FF , pFF , and FF_{id} as a function of SnO_x film thickness are summarized and plotted together in Fig. 6(c), which were calculated from the JV , pJV , and JV_{id} curves of representative devices (Fig. S2) with the detailed information listed in the [supplementary material](#) (Table S1). We observed that the ΔFF_{mid} increased from 2.6% for 5 nm to 2.9% for 10 nm, while for thicker SnO_x (15 nm), this value further increased to 3.9%. By comparing the trends of the two contributions to FF , $n_{id} > 1$ and R_s with increasing SnO_x film thickness, we found that ΔFF_{mid} increases with increasing SnO_x film thickness owing to increasing n_{id} . In contrast, ΔFF_{R_s} decreased with increasing film thickness. As the overall FF increased, the reduction in R_s was identified as the main reason for the improved FF with thicker SnO_x films. Lateral conductivity measurements were performed on bare SnO_x films in the dark, and the results are shown in Fig. 6(d). As the film thickness increased from 5 to 15 nm, the conductivity (σ) increased by two orders of magnitude, reducing the bulk resistance loss and subsequently improving the FF .

B. Band diagram

To understand the mechanism behind the improved conductivity of thicker SnO_x in the complete device, we visualized the band diagram of a cell with MeO-2PACz/perovskite/PEAI/C₆₀/SnO_x and examined its variation as the SnO_x film thickness increased from 5 to 15 nm. Ultraviolet photoelectron spectroscopy (UPS) measurements and numerical simulations using the drift-diffusion software SCAPS were conducted to obtain a deeper insight into band alignments, which have a significant impact on charge extraction and recombination. We prepared semi-devices for UPS measurements with a structure of ITO/MeO-2PACz/perovskite/C₆₀/SnO_x, employing 5, 10, and 15 nm SnO_x . The work function (Φ) was determined relative to the vacuum energy (E_{VAC}) from the UPS spectra by measuring the position of the cutoff at a high binding energy (E_B) using a linear fit at the background and steep edge (Fig. S3). The valence band (E_V) was determined by applying the same linear method to the leading edge of the UPS spectrum. The optical bandgap (E_g) of the SnO_x films with different thicknesses was calculated from Tauc plots of the function $(\alpha h\nu)^{1/2}$ vs photon energy ($h\nu$), which revealed a linear segment close to the absorption onset for amorphous and indirect bandgap semiconductors. The absorption coefficient³⁵ (α) was determined from $\alpha = 4\pi k/\lambda$ (Fig. S4), where k and λ are the extinction coefficient measured using ellipsometry and wavelength, respectively. The electron affinity (χ), which represents the energy difference between the conduction band (E_C) and E_{VAC} , was calculated using the measured E_V and E_g . These

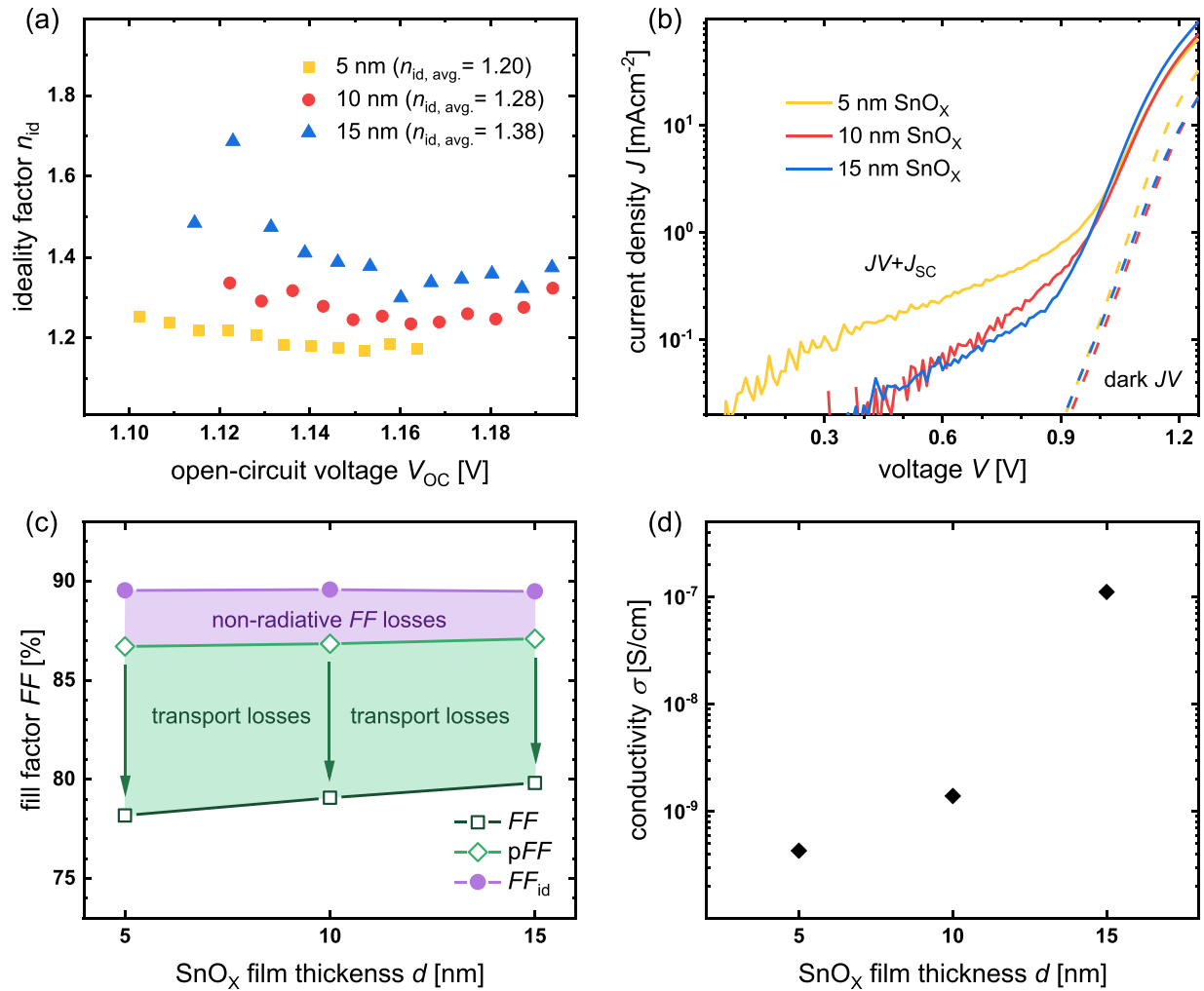


FIG. 6. (a) Ideality factor n_{id} derived from the Suns- V_{OC} measurement and the average value of n_{id} calculated from 1.1 V to the end of the measurement. (b) Illuminated (solid lines) and dark (dashed lines) JV curves of representative devices with increasing SnO_x film thickness plotted in the first quadrant. Thicker SnO_x films suppress carrier recombination at the ETL side, assuming that the recombination velocity at the HTL side is constant. (c) Comparison between the FF from the JV curves, the pFF from the pseudo-JV curves (measured on the same cells), and the FF_{id} from the ideal JV curves in the radiative limit considering the increasing SnO_x film thickness of the devices. (d) Lateral conductivity of the bare SnO_x films as a function of thickness. Thicker SnO_x films demonstrate enhanced conductivity and reduce the FF loss caused by bulk resistance.

measurements, along with the SCAPS simulations, provided valuable insight into how band alignment changes with SnO_x thickness, influencing charge dynamics within the device.

Figure 7(a) shows the energy levels of the valence band maximum (VBM), conduction band minimum (CBM), and Fermi energy at $E_{VAC} = 0$ eV for all layers in the PSCs studied in this work, where the E_g of 5 nm SnO_x was also set to 3.45 eV same as that of 10 and 15 nm SnO_x to keep it constant. It was observed that CBM and Φ remained almost constant as the SnO_x thickness decreased from 15 to 10 nm. However, when the layer thickness further decreased to 5 nm, the CBM moved upwards by 0.29 eV and the Φ moved downwards by ~ 0.11 eV, respectively.

To obtain the band diagram of the PSCs, we performed a preliminary simulation by inputting the experimentally measured energy levels of all the layers into the drift-diffusion simulation software SCAPS.

The parameters are given in Tables S2 and S3 in the [supplementary material](#), and the R_s was measured using J_{sc} and V_{oc} of the perovskite solar cells at different illumination intensities (Fig. S4). The successful convergence in solving Poisson's equations and boundary conditions allowed the acquisition of both band diagrams and JV curves. It is noteworthy that the CBM of C₆₀ has a pronounced influence on the band alignment, influencing the simulation outcomes, including FF . As previously discussed, χ was determined using the VBM (6.44 eV) obtained from UPS measurements (Fig. S4) and the E_g values from the literature, which range from 1.9 to 2.5 eV.^{36–39} This range causes the CBM to shift between 4.54 and 3.94 eV, resulting in, for instance, substantial changes in the potential gap of E_c at the C₆₀/SnO_x (5 nm) interface from a maximum of 470 meV to a minimum of 30 meV. To ensure reliable simulation outcomes, we performed systematic simulations to evaluate the reported E_g values of C₆₀. We compared the FF

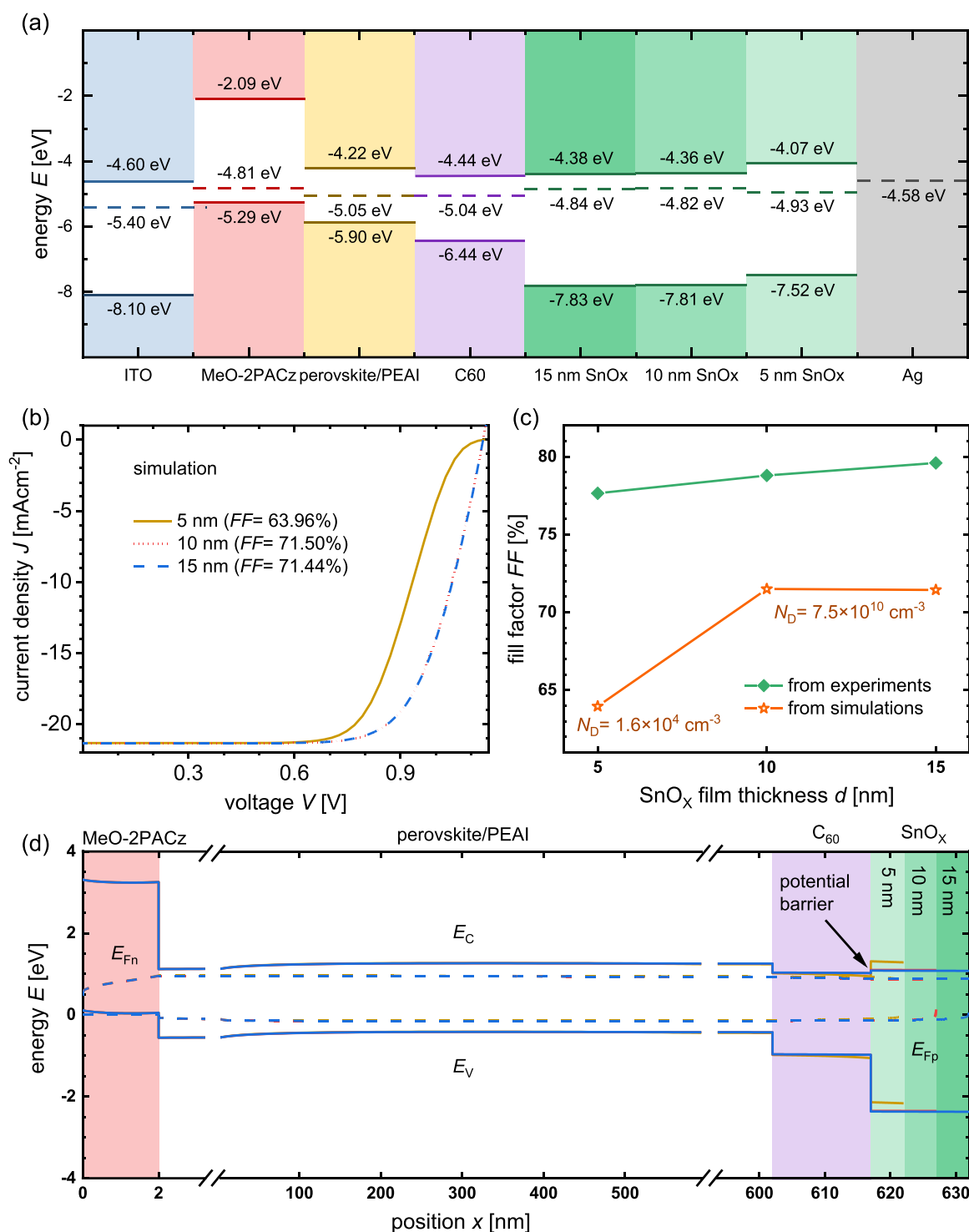


FIG. 7. (a) Schematic of the energy levels for all layers in opaque perovskite solar cells measured using UPS. (b) Comparison of simulated JV curves of opaque perovskite solar cells incorporating 5, 10, and 15 nm SnO_x extracted from SCAPS. (c) Experimentally measured and numerically simulated FF as a function of SnO_x film thickness; the doping concentration of SnO_x used in the simulations was calculated based on Eq. (6) and is indicated for each scenario. (d) Comparison of the simulated band diagram of an opaque perovskite solar cell with MeO-2PACz/perovskite/PEAI/C60/ SnO_x , incorporating increasing SnO_x film thickness, which is extracted at the maximum power point. A substantial discrepancy exists between experimental and simulated results.

values extracted from simulations using different E_g and χ values with the average FF values extracted from the experimental data (Fig. S5). The results demonstrate that an E_g of 2.0 eV for C_{60} is the most reasonable, as it closely aligns with both the absolute value and the trend of FF changes as a function of SnO_x thickness, matching real-world observations most accurately.

In the simulations, Φ was interpreted as the doping concentration (N_D), and the predicted JV curves for the three scenarios, using the experimentally measured energy levels, are shown in Fig. 7(b). For the 10 and 15 nm scenarios, we obtained diode JV curves similar to the experimental results. However, the presence of a non-diode JV curve for 5 nm suggests band misalignment in the simulation definition, primarily owing to the extremely shallow CBM of the 5 nm SnO_x compared to that of C_{60} . Figure 7(d) shows the simulated band diagrams, where we observed a pronounced potential barrier of 370 meV at the C_{60}/SnO_x (5 nm) interface, which hinders the extraction of charge carriers; therefore, the predicted value of the FF was below 70%.

We compared the average values of FF extracted from both the experiments and simulations as a function of the SnO_x film thickness, as shown in Fig. 7(c). In the experiments, the average FF value increased slowly by approximately 1% per thickness increment, whereas the first increment of 5 nm improved the FF by approximately 8% in the simulations owing to the transition from band misalignment to band alignment. The N_D of SnO_x layer used for the simulations were indicated additionally, which was calculated based on the energy gap between the Φ and χ measured by UPS using the following equation:

$$\phi = \chi + kT \ln \left(\frac{N_C}{N_D} \right), \quad (6)$$

where N_C is the effective density of states. When the SnO_x film thickness increased from 5 to 10 nm, N_D increased by six orders of magnitude but remained constant for further increments in thickness, which appears to be contradicting to expectations. Therefore, we used another method to evaluate the change in Φ with increasing SnO_x film thickness.

C. Space-charge-limited current (SCLC)

SCLC measurements are well known and are mostly used to determine the charge-carrier mobilities of intrinsic and lightly doped semiconductors.^{17,40} This measurement relies on the interpretation of the dark JV curves of single-carrier devices and electron- or hole-only devices under forward and reverse bias voltages. In a single-junction device, if the contact work functions are asymmetric at both ends, a built-in voltage (V_{BI}) is generated. A simple method was developed to extract the V_{BI} from SCLC JV data based on the Mott–Gurney (MG) law.^{41,42} Using the high-voltage assumption of $|V| \gg V_{BI}$, the V_{BI} in an single-carrier device with one semiconductor layer sandwiched between two asymmetric Ohmic contacts is given as¹⁷

$$V_{BI} = \frac{k_B T}{q} \ln \left(\frac{8 q N_C L^2 J_f}{9 \epsilon_r \epsilon_0 J_r} V^{-1} \right), \quad (7)$$

where $k_B T$ is the thermal energy. L is the thickness of the semiconductor layer being probed, which is C_{60} . $\epsilon_r \epsilon_0$ is the permittivity. V is the

applied voltage across the devices during the dark JV measurement. J_f/J_r is the ratio between the forward and reverse bias currents at the bias voltage.

We fabricated electron-only devices with a simple structure of glass/ITO/ ZnO nanoparticles/ $C_{60}/\text{SnO}_x/\text{Ag}$, in which only electrons dominate transport. Relative SCLC JV data were collected for this device, with the SnO_x film thickness as a variable and the other parameters as constants. A decisive advantage of SCLC relative to UPS is that it has an observable current ratio (J_f/J_r) that depends exponentially on the changes in V_{BI} , that is, the changes in Φ , because the UPS has a signal with a large error bar that depends linearly on the energy level. The errors in the energy level remain errors in the UPS and mess up the result, while in the SCLC, they end up in the $\ln(J_f/J_r)$ and are therefore much less dramatic. Furthermore, SCLC is a measurement inside a device that measures the difference in Φ in a situation where it is relevant, whereas UPS measures the surfaces of layers in vacuum. These surfaces are interfaces with other layers in the finished devices. The layers on top of the targeted surface alter the properties of the surface and corresponding interface to some extent. The only downside of SCLC is that it can only measure relative and not absolute values of the work function.

The SCLC JV curves of the electron-only devices with increasing SnO_x film thickness are shown in Figs. 8(a)–8(c), which were measured from -3 to 3 V and plotted on double logarithmic axes. The upper branch is the current for positive bias voltages from 0 to 3 V (forward bias), and the lower branch corresponds to negative bias voltages from -3 to 0 V (reverse bias). We observed that the vertical distance between the two branches increased for thicker SnO_x at a certain applied voltage, suggesting an increase in V_{BI} . Figure 8(d) shows a comparison of the ratio between the current densities at forward and reverse bias, where thicker SnO_x brought an increase in J_f/J_r at high voltages of above 1 V. By solving Eq. (7), the V_{BI} can be extracted from Fig. 8(d), and the results are shown in Fig. 8(e). The V_{BI} values were determined at a plateau for each curve. When the film thickness was increased from 5 to 10 and from 10 to 15 nm, V_{BI} increased, and the relative shifts (ΔV_{BI}) were 13 and 11 meV, respectively. Because ZnO nanoparticles have a higher Φ than SnO_x , this result demonstrates that the thicker the SnO_x , the closer it is to vacuum (lower Φ). Studies and experimental observations often show the thickness dependence of the work function in oxide semiconductor thin films and metallic films,^{43,44} which can be attributed to several factors: (1) The morphology and crystallinity of the film can change with thickness. Thicker films tend to have more bulk-like properties, while thinner films might be more amorphous, more susceptible to the properties of underlying films, or have different crystalline orientations, affecting the work function.⁴⁵ (2) The crystalline structure and defect density may also vary with film thickness, impacting the work function.⁴⁶ (3) In very thin films, quantum size effects (QSE) can alter the electronic band structure when the film thickness approaches the electron's de Broglie wavelength, affecting the work function.⁴⁷

D. Comparison to device simulations

We performed simulations based on the relative shift of Φ , which is equivalent to the ΔV_{BI} extracted from the SCLC JV curves, instead of the Φ measured by UPS, to reevaluate the impact of the changes in Φ on FF due to thickness variations of SnO_x . First, we treated the FF of the device employing 15 nm SnO_x as the starting point and adjusted

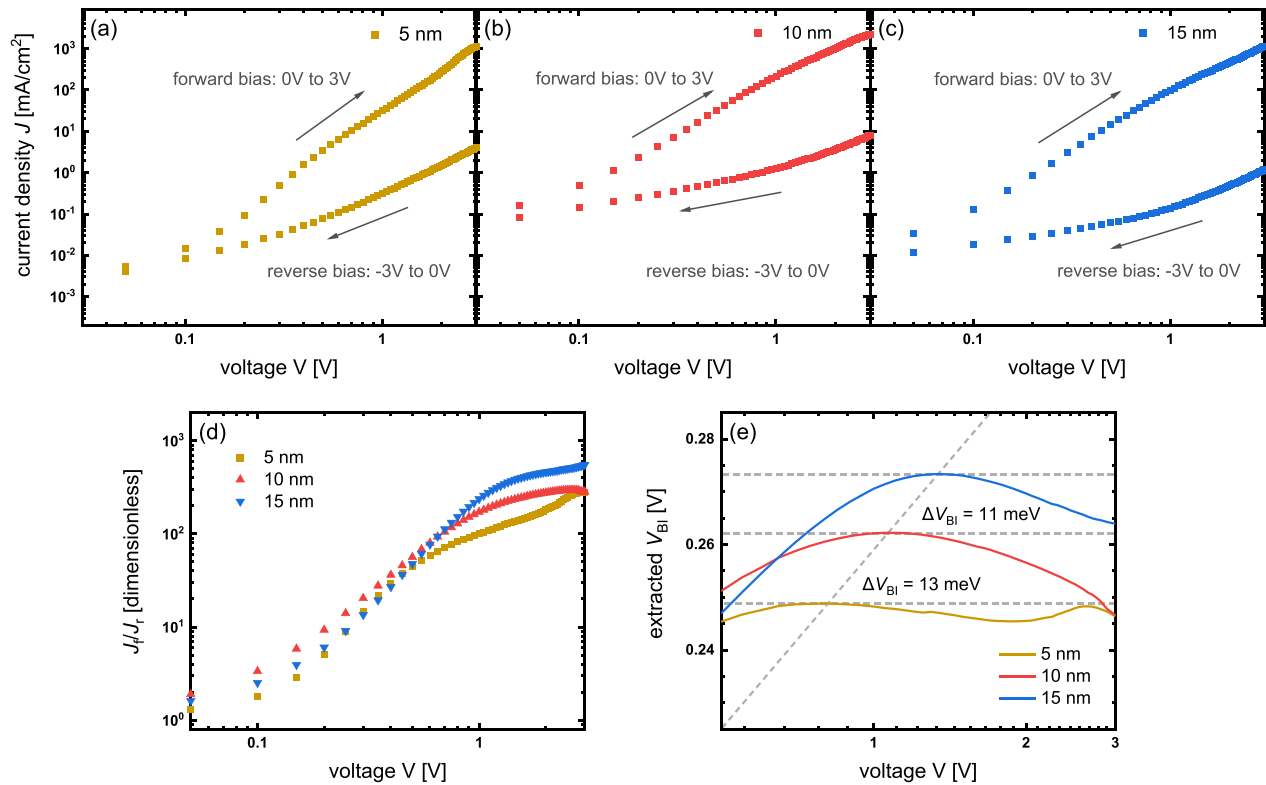


FIG. 8. SCLC JV curves of the representative electron-only devices with glass/ITO/ZnO nanoparticles/C₆₀/SnO_x/Ag incorporating (a) 5, (b) 10, and (c) 15 nm SnO_x. The lower branch is the measurement from -3 to 0 V (reverse current) and the upper branch is the measurement from 0 to 3 V (forward current) with the same step size of 0.05 V. (d) Comparison of the ratio between the current densities at forward and reverse bias with increasing SnO_x film thickness. (e) Extracted V_{BI} values obtained by fitting Eq. (7) to the ratio of experimentally measured SCLC JV curves. The implementation of thicker SnO_x films in the electron-only devices increases V_{BI} , suggesting a reduction in the work function of bare SnO_x as thickness increases.

the N_D in the simulations to ensure that the FF reached the same level as the experimental one. With this well-assumed N_D , Φ was calculated by solving Eq. (6). Here, the well-assumed value of N_D for 15 nm SnO_x is $3.2 \times 10^{17} \text{ cm}^{-3}$ and the value of the corresponding Φ is 4.44 eV. Third, we obtained Φ values of 10 and 5 nm SnO_x by adding the relative ΔV_{BI} to Φ of 15 nm, which were 4.45 and 4.46 eV, respectively. Finally, Φ was interpreted as N_D , $2.2 \times 10^{17} \text{ cm}^{-3}$ for 10 nm and $1.3 \times 10^{17} \text{ cm}^{-3}$ for 5 nm, and the calculated N_D values were input into the simulations to extract the FF s. A dotted-line plot of the variation in FF with thickness was drawn to compare the experimental values with the simulated values, as shown in Fig. 9(a). For the 5 nm scenario, the simulated FF overlapped perfectly with the experimental value, and a small gap of 0.57% was observed for 10 nm, which could be attributed to the scattering of experimental statistics. Therefore, our simulation results are in good agreement with the experimental results. The band diagrams were updated to the simulations and are partially shown in Fig. 9(b), where the heights of the three potential barriers at the C₆₀/SnO_x interface were all 60 meV because χ was kept constant in the simulations, regardless of the SnO_x film thickness. The energy gap between the CBM and the electron Fermi level (E_{Fn}) decreased as the film thickness increased, suggesting that a higher density of electrons were present in both the C₆₀ and SnO_x films. These results reveal the working mechanism behind the improved conductivity of the thicker

SnO_x in the complete device. Furthermore, our results are consistent with the theory that an increase in the built-in potential in a junction of a solar cell enhances its selectivity, i.e., its capability to collect the desired carrier species (electrons) and at the same time minimizes recombination losses for the holes.⁴⁸

Based on the above analysis of V_{OC} , J_{SC} , and FF , the SnO_x film thickness is likely to influence the recombination rate at a given carrier density at the perovskite/C₆₀ interface through the shift of equilibrium Fermi level. Initially, the increase in SnO_x film thickness reduces the work function of bare SnO_x, indicating that the Fermi level in SnO_x shifts up toward the vacuum energy as thickness increases. Subsequently, SnO_x exhibits a significantly lower work function compared to that of bare C₆₀, which moves the Fermi level at the perovskite/C₆₀ interface up toward the conduction band of C₆₀. We can assume that recombination at the perovskite/C₆₀ interface is dominated by interfacial SRH recombination with a rate $R_{int,SRH}$. The SRH recombination rate is described by a rational function as given by⁴⁹

$$R_{int,SRH} = \frac{np - n_i^2}{n/S_p + p/S_n}, \quad (8)$$

which produces a maximum recombination rate for a given product np of electron (n) and hole (p) densities on either side of the interface

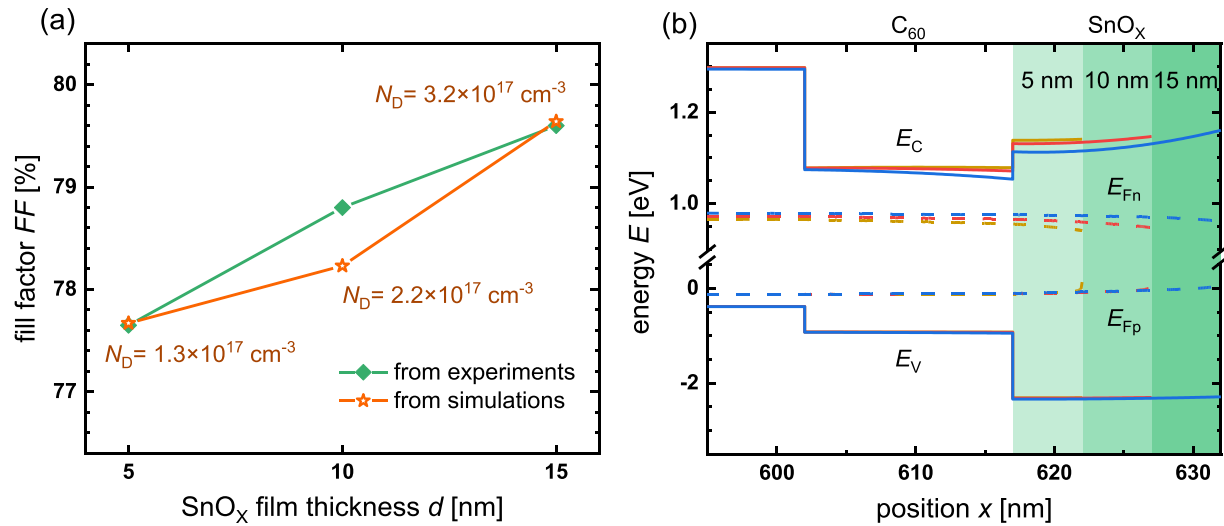


FIG. 9. (a) Experimentally measured and numerically simulated *FF* of opaque perovskite solar cells incorporating 5, 10, and 15 nm SnO_x, where the doping concentration of SnO_x used in the simulations was calculated using the built-in voltage extracted from the SCLC *JV* curves and is indicated for each scenario. In contrast to the previously observed significant *FF* discrepancy in Fig. 7(c), our simulation results are in good agreement with the experimental results. (b) Partial view of the simulated band diagram of an opaque perovskite solar cell with MeO-2PACz/perovskite/PEAI/C₆₀/SnO_x with increasing SnO_x film thickness extracted at the maximum power point, which allows for the analysis of the influence of SnO_x film thickness on carrier transport.

if the capture of electrons from the C₆₀ and holes from the perovskite by the interfacial trap is exactly equally likely. This condition can be expressed by the two terms in the denominator of Eq. (8) being equal ($n/S_p = p/S_n$) or by saying that the electron and hole capture rates must be equal ($S_n n = S_p p$). Here, S_n is the interfacial recombination velocity of electrons and S_p the interfacial recombination velocity of holes. This condition of avoiding similar capture rates is a fundamental and generic optimization criterion for solar cells^{50–52} and is for instance the reason why silicon solar cells benefit from smaller space charge region widths as this minimizes regions with similar electron and hole densities.⁵³ In this specific situation, we conclude that the shift in Fermi level due to the increase in SnO_x thickness is likely leading to a higher asymmetry in electron and hole densities on either side of the interface and thereby reduces the recombination rate at a given *np*-product without the need to reduce, e.g., the interfacial defect density which would directly enter the values of S_n and S_p .

VI. TANDEM SOLAR CELL PERFORMANCE

In our previous work,⁵ a semi-transparent perovskite solar cell with a 5 nm SnO_x exhibited a pronounced S-shaped *JV* curve, whereas increasing the thickness to 15 nm eliminated the S-shape. When the SnO_x film thickness decreased from 15 to 10 nm, the average efficiency decay exceeded 1% in the semi-transparent devices, which is greater than the average efficiency decay of approximately 0.4% in opaque devices, as shown in Figs. 1 and 2. This result demonstrates that in addition to the efficiency decay caused by the thickness reduction itself, the inadequate mitigation of sputter damage by a 10 nm SnO_x buffer layer is the primary factor in the efficiency decay of more than 1%. Moreover, our systemic investigation into the origin of sputter damage during ITO deposition has revealed that such damage generates vacancy defects within a few nanometers of the C₆₀ surface, as lattice carbon atoms are knocked out of the original sites by incident ions. Simultaneously, sputter damage results in the dissociation of C=N

bonds at the perovskite surface owing to phonon propagation. Nevertheless, the implementation of a SnO_x buffer layer with a critical thickness of 15 nm has been demonstrated to effectively mitigate this damage, thereby enhancing device performance by providing substantial protection to the perovskite/C₆₀ stack. The incorporation of a 5 or 10 nm SnO_x layer into perovskite/silicon tandem solar cells introduces additional variables beyond SnO_x film thickness that is sputter damage deteriorating the device performance and would not provide a valid comparison to the performance of the 15 nm counterpart. Therefore, in this work, we fabricated perovskite/silicon tandem solar cells using a 15 nm SnO_x buffer layer to mitigate sputter damage. Figures 10(a) and 10(b) show the *JV* curves for the champion cell with negligible hysteresis and the corresponding $Q_{e,PV}$ for the subcells, respectively. A laboratory-measured efficiency of 32.84% was achieved for an aperture area of 1 cm². The photogenerated current density for perovskite top cell ($J_{SC,pero}^{QE}$) and silicon bottom cell ($J_{SC,si}^{QE}$) were 21.55 and 20.11 mAcm⁻², respectively, suggesting that J_{SC} was limited by silicon bottom cell. We recalculated the *JV* curves (orange lines) using the J_{SC} derived from the $Q_{e,PV}$ of the silicon bottom cell, resulting in a corrected efficiency ($\eta_{corr} = (FF \cdot V_{OC})_{meas} \cdot \min(J_{SC,pero}^{QE}, J_{SC,si}^{QE})$) of 31.81%. Note that for the application of SnO_x buffer layer in perovskite/silicon tandem solar cells, 15 nm also outperforms 5 nm even if we do not consider the enhanced protection, it provides to the underlying organic films against sputtering-induced damage during the deposition of transparent conductive oxide. The superior performance of the tandem device arises primarily from the suppression of nonradiative recombination and better conductivity owing to the thicker SnO_x. To further improve the silicon bottom cell-limited J_{SC} , double-sided textured Czochralski wafers can be replaced with Float Zone wafers to enhance the optical response in the infrared spectrum.

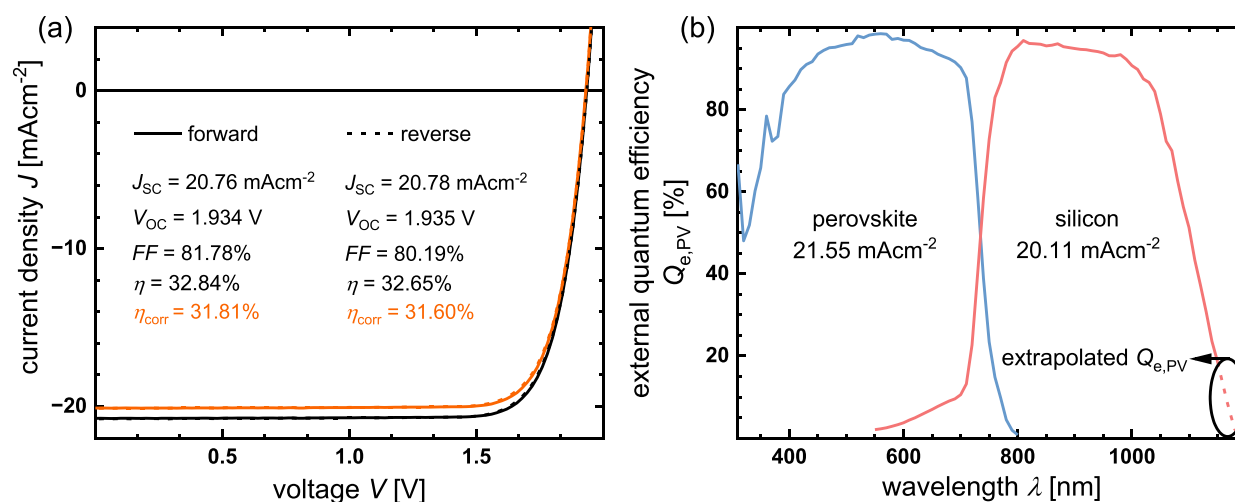


FIG. 10. (a) Measured and corrected JV curves for perovskite/silicon tandem solar cells incorporating 15 nm SnO_x buffer layer, where the performance parameters of forward and reverse sweep are provided. The corrected efficiency (η_{corr}) is recalculated by taking the $J_{\text{SC,Si}}^{\text{QE}}$ resulting from external quantum efficiency of the silicon bottom cell, which is currently the current-limiting subcell. The corrected JV curves are shifted up (to the lower J_{SC} of 20.11 mAcm^{-2}) which only has a tiny influence on the V_{OC} . (b) External quantum efficiencies $Q_{\text{e,PV}}$ for the perovskite top cell and silicon bottom cell. To improve the accuracy of the silicon quantum efficiency, it was extrapolated beyond 1150 nm using a simple model for the absorptivity of silicon as discussed in the method section.

VII. CONCLUSIONS

The present paper explains how the thickness of the SnO_x layer affects the photovoltaic parameters of single-junction perovskite solar cells and most likely also of perovskite top cells in highly efficient perovskite/silicon tandem solar cells. We discuss the changes in V_{OC} , J_{SC} , and FF of perovskite solar cells individually as a function of the thickness of SnO_x using both experimental and simulation methods. By analyzing the PL and $Q_{\text{e,PV}}$ results, thicker SnO_x layers, with fully developed physical properties like conductivity, suppress nonradiative interface recombination in completed devices. A comparison between the FF , pFF , and FF_{id} illustrates that thicker SnO_x improves the FF primarily through decreasing the series resistance of PSCs because thicker SnO_x films not only provide a better conductivity but also a more favorable band diagram in the perovskite/ C_{60} / SnO_x region. Therefore, the thicker SnO_x layers warrant an overall better selectivity of the contact for charge carrier collection. To demonstrate the latter point, UPS and SCLC measurements were performed to construct the band diagrams and to evaluate the thickness-dependent work function in practical situations. Both results reveal a shift in the work function of SnO_x with variation in the film thickness. Subsequent numerical device simulations demonstrate that the higher conductivity of thicker SnO_x films can be attributed to the presence of a higher density of electrons in both the C_{60} and SnO_x films, owing to a smaller energy barrier between the CBM and electron Fermi level, which reveals the working mechanism behind the FF improvement. Furthermore, the analysis of V_{OC} , J_{SC} , and FF demonstrates that the thicker SnO_x films reduce the recombination rate at the perovskite/ C_{60} interface due to the shift in Fermi level. The proper design of the SnO_x buffer layer has enabled the production of 32.84% efficient perovskite/silicon tandem solar cell (with a corresponding efficiency of 31.81% calculated using the J_{SC} from $Q_{\text{e,PV}}$).

SUPPLEMENTARY MATERIAL

See the [supplementary material](#) for the fabrication process of perovskite solar cells, characterization specifics of bare films, layer stacks, and complete devices, and list of parameters for drift-diffusion simulations using the software SCAPS. Further information supporting the findings of this work is provided, such as the SnO_x -dependent FF , JV curves, UPS spectra and bandgap data, the UPS spectra and bandgap of C_{60} , and the statistics of the performance of tandem solar cells.

ACKNOWLEDGMENTS

The authors thank Wilfried Reetz for technical assistance. We acknowledge funding by the Helmholtz Association via the POF IV funding, via the project “Beschleunigter Transfer der nächsten Generation von Solarzellen in die Massenfertigung—Zukunftstechnologie Tandem-Solarzellen,” via the Helmholtz.AI project AISPA—AI-driven instantaneous solar cell property analysis as well as by the Deutsche Forschungsgemeinschaft (German Research Foundation) via the project “Correlating Defect Densities with Recombination Losses in Halide-Perovskite Solar Cells.” Q.Y. is grateful for financial support from the China Scholarship Council (No. 202004910368).

AUTHOR DECLARATIONS

Conflict of Interest

The authors have no conflicts to disclose.

Author Contributions

Qing Yang: Conceptualization (lead); Data curation (lead); Formal analysis (equal); Investigation (lead); Methodology (equal); Software (equal); Validation (equal); Visualization (equal); Writing – original draft (lead); Writing – review & editing (equal). **Karsten Bittkau:**

Formal analysis (equal); Methodology (equal); Validation (equal); Writing – review & editing (equal). **Benjamin Klingebiel:** Formal analysis (equal); Investigation (equal); Software (equal); Visualization (equal); Writing – review & editing (equal). **Thomas Kirchartz:** Formal analysis (equal); Funding acquisition (equal); Methodology (equal); Project administration (equal); Resources (equal); Software (equal); Validation (equal); Visualization (equal); Writing – review & editing (equal). **Uwe Rau:** Formal analysis (equal); Investigation (equal); Project administration (equal); Resources (equal); Software (equal); Supervision (equal); Validation (equal); Writing – review & editing (equal). **Kaining Ding:** Formal analysis (equal); Funding acquisition (equal); Project administration (equal); Resources (equal); Supervision (equal); Visualization (equal); Writing – review & editing (equal).

DATA AVAILABILITY

The data that support the findings of this study are available from the corresponding author upon reasonable request.

REFERENCES

- S. Albrecht, M. Saliba, J. P. C. Baena, F. Lang, L. Kegelman, M. Mews, L. Steier, A. Abate, J. Rappich, and L. Korte, "Monolithic perovskite/silicon-heterojunction tandem solar cells processed at low temperature," *Energy Environ. Sci.* **9**, 81–88 (2016).
- E. Aydin, E. Ugur, B. K. Yildirim, T. G. Allen, P. Dally, A. Razaq, F. Cao, L. Xu, B. Vishal, A. Yazmaciyan, A. A. Said, S. Zhumagali, R. Azmi, M. Babics, A. Fell, C. Xiao, and S. De Wolf, "Enhanced optoelectronic coupling for perovskite/silicon tandem solar cells," *Nature* **623**, 732–738 (2023).
- See <https://www.nrel.gov/pv/cell-efficiency.html> for "NREL Transforming ENERGY"; accessed: November 2024.
- E. Aydin, C. Altinkaya, Y. Smirnov, M. A. Yaqin, K. P. S. Zanoni, A. Paliwal, Y. Firdaus, T. G. Allen, T. D. Anthopoulos, H. J. Bolink, M. Morales-Masis, and S. De Wolf, "Sputtered transparent electrodes for optoelectronic devices: Induced damage and mitigation strategies," *Mater.* **4**, 3549–3584 (2021).
- Q. Yang, W. Duan, A. Eberst, B. Klingebiel, Y. Wang, A. Kulkarni, A. Lambert, K. Bittkau, Y. Zhang, S. Vitusevich, U. Rau, T. Kirchartz, and K. Ding, "Origin of sputter damage during transparent conductive oxide deposition for semitransparent perovskite solar cells," *J. Mater. Chem. A* **12**, 14816–14827 (2024).
- M. Härtel, B. Li, S. Mariotti, P. Wagner, F. Ruske, S. Albrecht, and B. Szyszka, "Reducing sputter damage-induced recombination losses during deposition of the transparent front-electrode for monolithic perovskite/silicon tandem solar cells," *Sol. Energy Mater. Sol. Cells* **252**, 112180 (2023).
- K. A. Bush, A. F. Palmstrom, Z. J. Yu, M. Boccard, R. Cheacharoen, J. P. Mailoa, D. P. McMeekin, R. L. Z. Hoyer, C. D. Bailie, T. Leijtens, I. M. Peters, M. C. Minichetti, N. Rolston, R. Prasanna, S. Sofia, D. Harwood, W. Ma, F. Moghadam, H. J. Snaith, T. Buonassisi, Z. C. Holman, S. F. Bent, and M. D. McGehee, "23.6%-efficient monolithic perovskite/silicon tandem solar cells with improved stability," *Nat. Energy* **2**, 17009 (2017).
- M. Morales-Masis, S. De Wolf, R. Woods-Robinson, J. W. Ager, and C. Ballif, "Transparent electrodes for efficient optoelectronics," *Adv. Electron. Mater.* **3**, 1600529 (2017).
- S. Mariotti, E. Köhnen, F. Scheler, K. Sveinbjörnsson, L. Zimmermann, M. Piot, F. Yang, B. Li, J. Warby, A. Musienko, D. Menzel, S. K. Felix Lang, I. Levine, D. Mantione, A. Al-Ashouri, M. S. Härtel, K. Xu, A. Cruz, J. Kurpiers, P. Wagner, H. Köbler, J. Li, A. Magomedov, D. Mecerreyes, E. Unger, A. Abate, M. Stoltterfoht, B. Stannowski, R. Schlattmann, L. Korte, and S. Albrecht, "Interface engineering for high-performance, triple-halide perovskite-silicon tandem solar cells," *Science* **381**, 63–69 (2023).
- G. Nogay, F. Sahli, J. Werner, R. Monnard, M. Boccard, M. Despeisse, F. J. Haug, Q. Jeangros, A. Ingenito, and C. Ballif, "25.1%-efficient monolithic perovskite/silicon tandem solar cell based on a p-type monocrystalline textured silicon wafer and high-temperature passivating contacts," *ACS Energy Lett.* **4**, 844–845 (2019).
- F. Sahli, J. Werner, B. A. Kamino, M. Brauninger, R. Monnard, B. Paviet-Salomon, L. Barraud, L. Ding, J. J. Diaz Leon, D. Sacchetto, G. Cattaneo, M. Despeisse, M. Boccard, S. Nicolay, Q. Jeangros, B. Niesen, and C. Ballif, "Fully textured monolithic perovskite/silicon tandem solar cells with 25.2% power conversion efficiency," *Nat. Mater.* **17**, 820–826 (2018).
- K. A. Bush, S. Manzoor, K. Frohna, Z. J. Yu, J. A. Raiford, A. F. Palmstrom, H.-P. Wang, R. Prasanna, S. F. Bent, and Z. C. Holman, "Minimizing current and voltage losses to reach 25% efficient monolithic two-terminal perovskite-silicon tandem solar cells," *ACS Energy Lett.* **3**, 2173–2180 (2018).
- A. Al-Ashouri, E. Köhnen, B. Li, A. Magomedov, H. Hempel, P. Caprioglio, J. A. Márquez, A. B. Morales Vilches, E. Kasparavicius, and J. A. Smith, "Monolithic perovskite/silicon tandem solar cell with > 29% efficiency by enhanced hole extraction," *Science* **370**, 1300–1309 (2020).
- A. F. Palmstrom, J. A. Raiford, R. Prasanna, K. A. Bush, M. Sponseller, R. Cheacharoen, M. C. Minichetti, D. S. Bergsman, T. Leijtens, H. P. Wang, V. Bulović, M. D. McGehee, and S. F. Bent, "Interfacial effects of tin oxide atomic layer deposition in metal halide perovskite photovoltaics," *Adv. Energy Mater.* **8**, 1800591 (2018).
- Z. Yu, Z. Yang, Z. Ni, Y. Shao, B. Chen, Y. Lin, H. Wei, Z. J. Yu, Z. Holman, and J. Huang, "Simplified interconnection structure based on C_{60}/SnO_{2-x} for all-perovskite tandem solar cells," *Nat. Energy* **5**, 657–665 (2020).
- M. Burgelman, P. Nollet, and S. Degraeve, "Modelling polycrystalline semiconductor solar cells," *Thin Solid Films* **361–362**, 527–532 (2000).
- J. A. Röhr, "Direct determination of built-in voltages in asymmetric single-carrier devices," *Phys. Rev. Appl.* **11**, 054079 (2019).
- T. Kirchartz, J. A. Márquez, M. Stoltterfoht, and T. Unold, "Photoluminescence-based characterization of halide perovskites for photovoltaics," *Adv. Energy Mater.* **10**, 1904134 (2020).
- U. Rau, "Reciprocity relation between photovoltaic quantum efficiency and electroluminescent emission of solar cells," *Phys. Rev. B* **76**, 085303 (2007).
- R. T. Ross, "Some thermodynamics of photochemical systems," *J. Chem. Phys.* **46**, 4590–4593 (1967).
- W. Shockley and H. J. Queisser, "Detailed balance limit of efficiency of p-n junction solar cells," *J. Appl. Phys.* **32**, 510–519 (1961).
- D. F. Swinehart, "The Beer-Lambert law," *J. Chem. Educ.* **39**, 333 (1962).
- Q. Yang, K. Bittkau, A. Eberst, U. Rau, and K. Ding, "The impact of interface recombination on the external quantum efficiency of silicon solar cells," *Sol. Energy Mater. Sol. Cells* **273**, 112953 (2024).
- C. Chen, S. Zhang, S. Wu, W. Zhang, H. Zhu, Z. Xiong, Y. Zhang, and W. Chen, "Effect of BCP buffer layer on eliminating charge accumulation for high performance of inverted perovskite solar cells," *RSC Adv.* **7**, 35819–35826 (2017).
- N. Shibayama, H. Kanda, T. W. Kim, H. Segawa, and S. Ito, "Design of BCP buffer layer for inverted perovskite solar cells using ideal factor," *APL Mater.* **7**, 031117 (2019).
- I. Miccoli, F. Edler, H. Pfnur, and C. Tegenkamp, "The 100th anniversary of the four-point probe technique: The role of probe geometries in isotropic and anisotropic systems," *J. Phys. Condens. Matter* **27**, 223201 (2015).
- M. A. Green, "Accuracy of analytical expressions for solar cell fill factors," *Sol. Cells* **7**, 337–340 (1982).
- T. Kirchartz, F. Deledalle, P. S. Tuladhar, J. R. Durrant, and J. Nelson, "On the differences between dark and light ideality factor in polymer: Fullerene solar cells," *J. Phys. Chem. Lett.* **4**, 2371–2376 (2013).
- K. Tvingstedt and C. Deibel, "Temperature dependence of ideality factors in organic solar cells and the relation to radiative efficiency," *Adv. Energy Mater.* **6**, 1502230 (2016).
- Y. Yuan, G. Yan, C. Dreessen, T. Rudolph, M. Hulsbeck, B. Klingebiel, J. Ye, U. Rau, and T. Kirchartz, "Shallow defects and variable photoluminescence decay times up to 280 micros in triple-cation perovskites," *Nat. Mater.* **23**, 391 (2024).
- M. Stoltterfoht, C. M. Wolff, J. A. Márquez, S. Zhang, C. J. Hages, D. Rothhardt, S. Albrecht, P. L. Burn, P. Meredith, T. Unold, and D. Neher, "Visualization and suppression of interfacial recombination for high-efficiency large-area pin perovskite solar cells," *Nat. Energy* **3**, 847–854 (2018).
- P. Würfel, *Physics of Solar Cells* (Wiley-VCH, 2005).

- ³³F. Peña-Camargo, J. Thiesbrummel, H. Hempel, A. Musiienko, V. M. Le Corre, J. Diekmann, J. Warby, T. Unold, F. Lang, D. Neher, and M. Stollerfoht, "Revealing the doping density in perovskite solar cells and its impact on device performance," *Appl. Phys. Rev.* **9**, 021409 (2022).
- ³⁴D. Grabowski, Z. Liu, G. Schöpe, U. Rau, and T. Kirchartz, "Fill factor losses and deviations from the superposition principle in lead halide perovskite solar cells," *Sol. RRL* **6**, 2200507 (2022).
- ³⁵M. N. Mullings, C. Häggglund, and S. F. Bent, "Tin oxide atomic layer deposition from tetrakis(dimethylamino)tin and water," *J. Vac. Sci. Technol. A* **31**, 061503 (2013).
- ³⁶D. Menzel, A. A. Ashouri, A. Tejada, I. Levine, J. A. Guerra, B. Rech, S. Albrecht, and L. Korte, "Field effect passivation in perovskite solar cells by a LiF interlayer," *Adv. Energy Mater.* **12**, 2201109 (2022).
- ³⁷K. Akaike, K. Kanai, H. Yoshida, J. Tsutsumi, T. Nishi, N. Sato, Y. Ouchi, and K. Seki, "Ultraviolet photoelectron spectroscopy and inverse photoemission spectroscopy of [6, 6]-phenyl-C₆₁-butyric acid methyl ester in gas and solid phases," *J. Appl. Phys.* **104**, 023710 (2008).
- ³⁸P. Schulz, L. L. Whittaker-Brooks, B. A. MacLeod, D. C. Olson, Y. L. Loo, and A. Kahn, "Electronic level alignment in inverted organometal perovskite solar cells," *Adv. Mater. Interfaces* **2**, 1400532 (2015).
- ³⁹Z.-L. Guan, J. B. Kim, H. Wang, C. Jaye, D. A. Fischer, Y.-L. Loo, and A. Kahn, "Direct determination of the electronic structure of the poly(3-hexylthiophene): phenyl-[6,6]-C₆₁ butyric acid methyl ester blend," *Org. Electron.* **11**, 1779–1785 (2010).
- ⁴⁰J. Siekmann, A. Kulkarni, S. Akel, B. Klingebiel, M. Saliba, U. Rau, and T. Kirchartz, "Characterizing the influence of charge extraction layers on the performance of triple-cation perovskite solar cells," *Adv. Energy Mater.* **13**, 2300448 (2023).
- ⁴¹N. F. Mott and R. W. Gurney, *Electronic Processes in Ionic Crystals* (Clarendon Press, Oxford, 1940).
- ⁴²M. A. Lampert and R. B. Schilling, *Semiconductors and Semimetals* (Elsevier, 1970), Vol. 6.
- ⁴³O. Çiçek, S. Kurnaz, A. Bekar, and Ö. Öztürk, "Comparative investigation on electronic properties of metal-semiconductor structures with variable ZnO thin film thickness for sensor applications," *Composites B* **174**, 106987 (2019).
- ⁴⁴F. Schulte, "A theory of thin metal films: Electron density, potentials and work function," *Surf. Sci.* **55**, 427–444 (1976).
- ⁴⁵K. Choi, H.-C. Wen, H. Alshareef, R. Harris, P. Lysaght, H. Luan, P. Majhi, and B. Lee, in Presented at the Proceedings of 35th European Solid-State Device Research Conference (2005).
- ⁴⁶V. Nádaždy, K. Gmucová, P. Nádaždy, P. Siffalovic, K. Vegso, M. Jergel, F. Schauer, and E. Majkova, "Thickness effect on structural defect-related density of states and crystallinity in P3HT thin films on ITO substrates," *J. Phys. Chem. C* **122**, 5881–5887 (2018).
- ⁴⁷J. Chrzanowski and B. Bieg, "Thickness dependence of the work function in case of ultra-thin metallic layers," *Appl. Surf. Sci.* **540**, 148363 (2021).
- ⁴⁸U. Rau and T. Kirchartz, "Charge carrier collection and contact selectivity in solar cells," *Adv. Mater. Interfaces* **6**, 1900252 (2019).
- ⁴⁹J. Haddad, B. Krogmeier, B. Klingebiel, L. Krückemeier, S. Melhem, Z. Liu, J. Hüpkens, S. Mathur, and T. Kirchartz, "Analyzing interface recombination in lead-halide perovskite solar cells with organic and inorganic hole-transport layers," *Adv. Mater. Interfaces* **7**, 2000366 (2020).
- ⁵⁰T. Kirchartz, J. Bisquert, I. Mora-Sero, and G. Garcia-Belmonte, "Classification of solar cells according to mechanisms of charge separation and charge collection," *Phys. Chem. Chem. Phys.* **17**, 4007–4014 (2015).
- ⁵¹J. Hüpkens, U. Rau, and T. Kirchartz, "Dielectric junction: Electrostatic design for charge carrier collection in solar cells," *Sol. RRL* **6**, 2100720 (2022).
- ⁵²B. Das, Z. Liu, I. Aguilera, U. Rau, and T. Kirchartz, "Defect tolerant device geometries for lead-halide perovskites," *Mater. Adv.* **2**, 3655–3670 (2021).
- ⁵³M. Stocks, A. Cuevas, and A. Blakers, "Theoretical comparison of conventional and multilayer thin silicon solar cells," *Prog. Photovoltaics: Res. Appl.* **4**, 35–54 (1996).